

Exchange and Microviscosity of Dynamic Nanocompartments

Romana Shathy,¹ Alexandria Guinness,¹ and John M. Franck¹

¹*Department of Chemistry, Syracuse University, Syracuse, NY 13210, USA**

(Dated: Tuesday 15th October, 2024)

reverse micelles (RMs) provide a controlled system for studying the unique structural and dynamic behaviors of confined water, thus gaining a general insight into the behavior of water under confinement and at interfaces. This study employs Electron Spin Resonance (ESR) to study the dynamics inside RMs and capitalizes on the fact that different preparations of RMs can precisely manipulate both the size of water pools as well as whether or not different pools can come into contact. A small spin label moiety, less than a half nanometer in size tumbles in solution, offering insight into the rotational diffusion from room temperature down to deeply super-cooled temperatures. Two different spin probes can separately probe the dynamics of the interfacial layer *vs.* those at the core of the reverse micelle. The results provide critical insights into how thermodynamic transitions affect the stability and behavior of water in confined spaces, enhancing the understanding of nucleation and ice crystal growth, as well as the broader understanding of confined water's role in various chemical and biological systems. The ability to more precisely understand and control reaction dynamics and thermodynamics inside confined aqueous systems across a broad range of temperatures will prove useful to fields ranging from biophysics to the development of new nano-materials.

I. Introduction

Water, when confined, exhibits unique structural, dynamic, and thermodynamic characteristics that differ markedly from its behavior in bulk, making it an important subject for study¹⁻⁵. Such confinement requires a macromolecular container that limits the water to nanoscopic volumes. reverse micelles (RMs), *i.e.* containers built of surfactant dispersed in an apolar solvent, prove crucial for various applications in chemistry, biophysics,^{1,6-10} and drug delivery⁷. They not only confine water within nanoscopic spaces but also possess the unique ability to undergo fusion-fission processes¹⁰⁻¹³, along with tumbling and translational motion. Thus RMs serve as *dynamic* nanocontainers. The interplay between the internal molecular dynamics and the dynamics of the nanocontainers themselves offers potential for manipulating the content and stability of guest molecules or reactions contained within.

Electron Spin Resonance (Electron Spin Resonance (ESR)) offers detailed insights into the dynamics of the local environments surrounding specially placed spin probes, and this tool has been used to specifically study confined environments¹⁴. For example, it has studied the hydration layer of proteins in frozen solvent¹⁵. ESR has also probed polymers, such as hydrogels or polymeric membranes^{16 ? ?}, and even complex nanostructures⁷. ESR has also been utilized to explore the dynamics of bulk water at deeply supercooled temperatures¹⁷. Furthermore, research has demonstrated that the rotational motion of a spin probe becomes decoupled from the viscosity of bulk water at 277 K, with the activation energy for the spin probe's rotation being higher than that of water's viscosity below this temperature¹⁸.

In previous work, ESR investigated both the mo-

bility of surfactants and the dynamics of the aqueous environment within reverse micelles. Previous literature⁷ employed the 4-SLBA (4-(2-n-undecyl-3-oxyl-4,4,-dimethyloxazolidin-2-yl) butyric acid) spin probe to study the mobility of the alkyl sidechains of the surfactant. Literature going back a few decades agrees with the idea that the mobility of a spin probe captured inside an RM decreases as the size of the RM decreases⁸. Other early studies showed that the mobility of the spin label changes as a function of the water loading¹⁹, and introduced a core-shell model of bulk water surrounded by interfacial/bound water to explain the correlation times observed⁸. Some of this early work even employs spin labels to look at the changing rotational correlation time of spin probes inside RMs as w_0 changes^{8,19}; in other words, what today would be understood as microviscosity. Tbl. I further extends the analysis by applying a standard linewidth analysis^{9,20} (eq. 1) to the spectra presented in^{8,19}, in order to determine the rotational diffusion as a function of water loading. This analysis makes it clear that the rotational diffusion of the surfactant-water interface spin label CAT-16 is slower than the aqueous spin label DSTA. Furthermore, it illustrates that a decrease in the water loading (w_0) further decreases the rotational correlation time. Finally, by reporting on the local polarity, this previous work demonstrates (see fig. S1) how the hyperfine splitting helps to determine the location of the spin label within a RM¹⁹.

However, challenges and contradictions remain in understanding the behavior of encapsulated water in RMs. Early work on the ESR of RMs, including studies using hydroxytempo, faced challenges due to the equilibrium of spin labels between the water, surfactant layer, and apolar dispersant²¹. Previous studies²², also indicated that the rotational diffusion of spin labels follows Arrhenius temperature dependence at low water loading (see fig. S2)⁷. This observation seems to conflict with the well documented nonlinearities in the viscos-

* jmfranck@syr.edu

ity of water as the temperature is lowered from room temperature down to the dynamic crossover temperature near 222-225 K¹. A review of phase transitions of the water inside RMs reveals an interesting conflict. DSC studies²³ report the freezing of water at temperatures near the entry into what is now known as “no-man’s land” near 230 K¹ (specifically, DSC observed a transition at a slightly higher temperature, -41°C). This freezing only affects a sub-population of the water; in particular, freezing only occurs for $w_0 \geq 7$ and the enthalpy of fusion per mole of water grows with w_0 ²³. To the authors’ knowledge, ESR had not previously reported on this transition inside RMs, despite the fact ESR has been used to explore the liquid water in fissures of ice inside “no man’s land”¹⁷. In contrast, Nuclear Magnetic Resonance (NMR) studies⁶, indicate the freezing of water at the much higher temperature of 243 K. Earlier reports used ESR to observe a similar effect²¹. In the current study, ESR investigates both sample systems to offer insight into the reasons for the discrepancy.

The present study employs specialized spin probes to retrieve unique insights about the behavior of dynamic nanocontainers such as RMs. Two types of spin labels are employed: one (TEMPO-SO₄) located in the middle of the RM and another (CAT-16) in the interfacial layer between the water and the surfactant. This study analyzes ESR spectra to measure the microviscosity inside these nanocontainers over wide temperature ranges. The present research investigated the mobility of two spin labels using isooctane (melting point: -107.3°C \approx 166 K) and dodecane (melting point: -10°C \approx 263 K) as solvents. The study of RMs in isooctane provides the information of mobility of RM and spin label over a wide temperature range, and presents a new view on the process of cold-shedding of water. In contrast, when the dodecane freezes, it immobilizes the RM. This provides the opportunity to distinguish between the mobility of the RM and spin label. As proves more important, it also suppresses fusion and fission of the RM aggregates.

The approach presented in the current article builds on these foundations by using an anionic spin label that remains within the water core, providing a clearer picture of the water dynamics within these dynamic nanocontainers, and capitalizing on modern data-processing tools, as well as spectroscopic simulation tools that offer more detailed and reliable descriptions of the spin label motion. The majority of this article utilizes a relatively qualitative analysis of temperature-dependent studies of RMs as a tool to bring together various disparate observations from the literature and to paint a coherent picture of how the water inside RMs responds to changes in temperature. Simulations are utilized to explore the behavior of the spin label when the situation becomes more complicated, in particular where the water inside the RMs is supercooled.

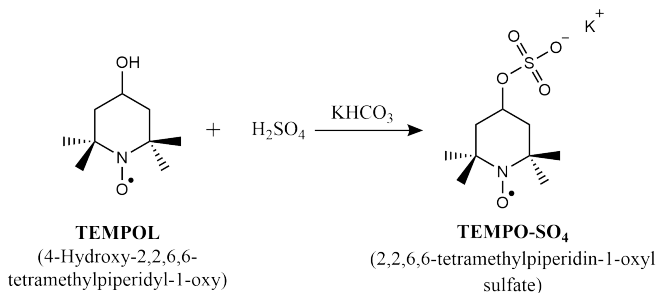


FIG. 1. Synthesis of TEMPO-SO₄

II. Experimental

II.1. ESR

All EPR measurements were recorded at X-band (microwave frequency 9.4 GHz to 9.8 GHz) on a Bruker ELEXSYSII E500 spectrometer equipped with a Bruker ER 4122 super-high Q (SHQE) resonator and SuperX bridge. A variable-temperature accessory ER 4141VT enabled variable temperature EPR measurements. In-house python scripts (based on pyspecdata²⁴) directly read, process, and plot the XEPR-format spectral files, as well as export to ascii and extract the resonance frequency for subsequent analysis in Altenbach’s Multicomponent program; similarly EasySpin can directly read the XEPR-format files. (Note that both Multicomponent and EasySpin employ variants of the “NLSL” program from the Freed lab²⁵.)

II.2. Synthesis

II.2.A. Synthesis of TEMPO-SO₄

The aqueous spin probe TEMPO-SO₄ (2,2,6,6-tetramethylpiperidin-1-oxyl sulfate) was synthesized through the sulfation of TEMPOL (4-Hydroxy-2,2,6,6-tetramethylpiperidin-1-oxyl) following literature procedure²⁶:

5 g (29.03 mmol) of TEMPOL ($\geq 98\%$, Toronto Research Chemicals) was pestled, added slowly to 35 mL of concentrated sulfuric acid, and stirred for 20 minutes at room temperature. The reaction mixture was then added dropwise to 250 mL of 1.3 M KHCO₃ solution. The aqueous phase was washed in an extraction funnel 5 \times with 50 mL of ethyl acetate ($\geq 99.5\%$, Thermo Scientific). The water was then removed with a rotary evaporator. The resulting yellow sticky solid was added to 30mL acetone (HPLC grade, Fisher Scientific) and stirred until only colorless solid remained. After vacuum filtration, most acetone in the filtrate was removed *via* rotary evaporation. The resulting dark orange oil, after sitting for 72 hours in a desiccator under reduced pressure, in the dark, became a dark red solid (TEMPO-SO₄). Some of this TEMPO-SO₄ was dissolved in DMSO-d₆ (99.9%, Cambridge Isotope Laboratories) with a drop of phenyl hydrazine (97%, Acros Organics) to enable NMR (fig. S3): ¹H NMR (DMSO-d₆, quenched with phenyl hydrazine, 400 MHz): δ 1.04 (d, 12H), 1.31 (t, 2H), 1.92-1.97 (m,

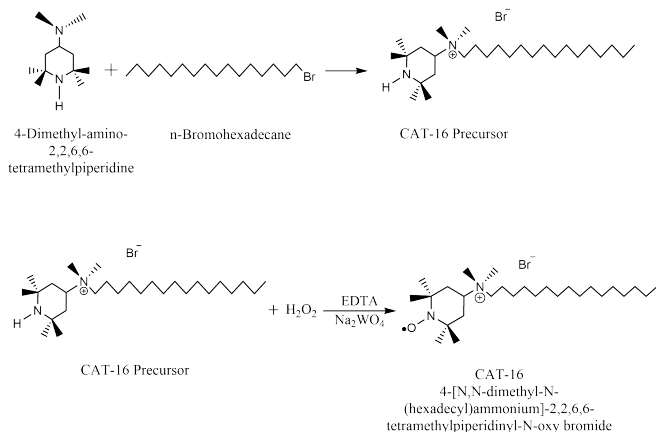


FIG. 2. Synthesis reaction of CAT-16

2H), 4.32 (tt, 1H). A different aliquot was dissolved in water for ESR spectroscopy that verified the presence of nitroxide.

II.2.B. Synthesis of CAT-16

The amphiphilic spin label CAT16 (4-[N,N-dimethyl-N-(hexadecyl)ammonium]-2,2,6,6-tetramethylpiperidiny-N-oxy bromide) incorporates into the surfactant-water interface of the RM. A protocol for the routine synthesis and purification of CAT16 was developed based on previous literature^{19,27,28}. It involves two steps: alkylation and oxidation.

Alkylation: 1 mL (3.34 mmol) of 4-dimethyl-amino-2,2,6,6-tetramethylpiperidine (Santa Cruz Biotechnology) was added to 1.25 mL (4.06 mmol) of bromohexadecane (98%, Alfa Aesar) in a round bottom flask. The mixture was heated in an oil bath at 75°C for 24 hours under vigorous stirring in the dark, under nitrogen flow. Following trituration with 15 mL hexane (95%, Aldrich Chemical Company) and vacuum filtration, the resulting solid retentate was washed three times with 10 mL diethyl ether ($\geq 99.8\%$, Sigma-Aldrich) to remove any side products, yielding 0.392 g (0.8 mmol) white powder labeled as “CAT-16 precursor” (fig. 2, 4-Piperidinaminium, N-hexadecyl-N,N,2,2,6,6-hexamethyl bromide).

Oxidation: The CAT-16 precursor (0.8 mmol, 0.392 g) was dissolved in 5 mL methanol (HPLC grade, Fisher Chemical) to which 0.5 mL (2.21 mmol) 15% H₂O₂ (Macron Fine Chemicals) was added dropwise in the presence of 24 mg (0.07 mmol) sodium tungstate oxide dihydrate ($\geq 95\%$, Alfa Aesar) and 23 mg (0.06 mmol) EDTA disodium salt dihydrate (99%, grade, Fisher Chemical), while the solution pH was maintained at 10 (with NaOH, Fisher Scientific). The concentration of H₂O₂ was verified using peroxide test strips from Bartovation (Item model number: PPX01V50), which are sensitive up to 10% H₂O₂ (dilution allows accurate measurement of higher concentrations). The reaction progress was monitored each day with TLC (solvent: CHCl₃:MeOH:H₂O 13:5:1 v:v:v); visualization: combined I₂ and UV; Chloroform: ACS grade $\geq 99.8\%$,

Sigma-Aldrich; Methanol: HPLC grade, Fisher chemical). Additional H₂O₂ was added in 0.25 mL (1.1 mmol) increments until completion of reaction while maintaining pH 10. In total 1.5 mL (6.62 mmol) H₂O₂ was added over four days, and a mild yellow/brown colored liquid oil was formed. (Note that the amounts and concentration of H₂O₂ mentioned above are the actual tested values.) On the fifth day, the reaction mixture was extracted 2× with 20 mL dichloromethane (HPLC grade, Thermo Scientific) and dried over anhydrous magnesium sulfate (Bio Basic). After rotary evaporation, a reddish-orange thick oil remained; this solidified after two hours when placed in a desiccator under vacuum. After 2× trituration with 30 mL hexane, centrifugation, and multiple recrystallizations from a mixture of dichloromethane and hexane, pure salmon-colored CAT-16 was obtained. Dissolution in DMSO-d₆ (99.9%, Cambridge Isotope Laboratories) with a drop of phenyl hydrazine (97%, Acros Organics) enabled NMR at 800 MHz (fig. S4): ¹H NMR (DMSO-d₆, quenched with phenyl hydrazine, 800 MHz): δ 0.86 (t, 3H), 1.08-1.14 (d, 12H), 1.25 (m, 29H), 1.63 (m, 4H), 1.94 (d, 2H), 2.96 (s, 6H), 3.23 (m, 2H), 3.58 (t, 1H). ESR of CAT-16 dissolved in 90:10 v:v Chloroform:Methanol confirmed the presence of the nitroxide group.

II.3. RM preparation

A stock solution of 100 mM TEMPO-SO₄ (0.498 mmol, 0.145 g, fig. 1) in 5 mL ultrapure water (Millipore Milli-Q system) was prepared. Additionally, a stock solution of 2.03 mM CAT-16 (0.204 mmol, 0.103 g, fig. 2) in 100 mL chloroform:methanol (90:10) (Chloroform: ACS grade $\geq 99.8\%$, Sigma-Aldrich, Methanol: HPLC grade, Fisher Chemical) was prepared. The TEMPO-SO₄ solution was diluted with ultrapure water to the desired concentration for individual preparations. Stock solution in CHCl₃:MeOH solvent were stored at -20°C, while aqueous stocks were stored at 4°C. Next, a solution of 0.300 M Aerosol-OT (AOT) surfactant (Dioctyl sulfosuccinate sodium salt, $\geq 97\%$, Sigma-Aldrich, 1.50 mmol, 0.667 g) was prepared in 5 mL dispersant in either isooctane (2,2,4-Trimethylpentane, Alfa Aesar) or in dodecane (n-Dodecane $\geq 99.8\%$, Thermo Scientific).

To prepare 200 μ L RM with CAT-16, first, the desired amount of stock solution (typically 49.2 μ L yielding 100×10^{-9} mol CAT-16) was dried in a dry culture tube under a flow of dry nitrogen before adding 100 μ L of 0.300 M AOT in dispersant and vortexing. Alternately, for the TEMPO-SO₄ RM, 100 μ L of 0.300 M AOT (30.0 μ mol) in dispersant was added to a clean, dry culture tube (without CAT16). In either case, to achieve the required water loading ($w_0 = \text{mol H}_2\text{O}/\text{mol AOT}$; $3 \leq w_0 \leq 40$), between 1.62 μ L (90.0 μ mol H₂O) and 21.6 μ L (1.20 mmol H₂O) of aqueous solution was added. (Note that the ratio of the moles of water molecules to the aqueous solution volume was assumed to be unchanged, at 55.5 M, for the TEMPO-SO₄ solution).

Finally, the solution was diluted with pure dispersant

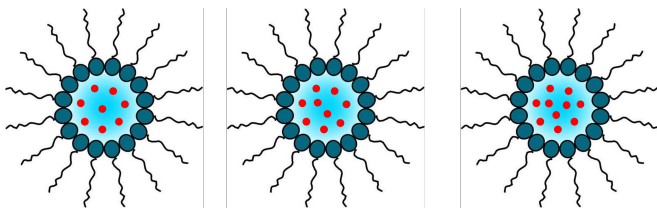


FIG. 3. When loaded with aqueous solution of spin probes (shown in red here, in numbers appropriate for $w_0 = 20$ and local concentration of 100 mM) RMs aggregates exhibit a range of local concentrations, from low (left) to high (right). The different local concentrations result in signals with different Heisenberg exchange rates.

to a total volume of 200 μL , then vortexed (for repeated 60 s intervals, continuing until transparent – typically 15 min). In all instances, the concentration of moles of AOT per total RM solution was maintained at 150 mM. The RM samples equilibrated at room temperature for 30 minutes. Each 20.0 μL sample was loaded into a glass capillary tube (0.704 mm i.d. 1.20 mm o.d.) and held inside the end of a larger capillary so that it was directly exposed to the flow of cold gas in the center of the cavity.

III. Results and Discussion

III.1. Heisenberg Exchange Responds to Segregation of the Aqueous Solution

First, briefly note that, at high spin probe concentration, Heisenberg Exchange leaves a distinctive signature on the spectra arising from the segregation of the aqueous solution into the nanocompartments. For example, very high concentration TEMPO-sulfate spin probes loaded into RMs yield a spectrum that changes significantly upon changes in water loading (w_0), as shown in fig. 4 and fig. 5. These changes arise from differing distributions of local concentrations inside the RM at the two different w_0 . Specifically, subdivision of the aqueous solution into nanocompartments yields a variation of the local concentration inside each nanocompartment, since even at high concentration, each RM compartment/aggregate will include, at most, tens of individual spin probe molecules (fig. 3). In fact, a simple Poisson distribution analysis (fig. 6) suggests that when a 100 mM spin probe solution is added to the surfactant to create an RM of $w_0 = 20$, the local concentration of spin probe inside the RM frequently varies significantly from the average concentration. Each different local concentration results in a differing rate of spin probe collisions, Heisenberg exchange, and therefore ESR linewidth.

In particular, note that individual RMs with high local concentration (near to 100 mM and greater) and correspondingly rapid Heisenberg exchange contribute to the broad central hump in fig. 5 and fig. 4. When some population of RMs with lower local concentrations are present, they contribute spectra that have slower Heisenberg exchange and are better resolved into three individual hyperfine components. Because these contributions have

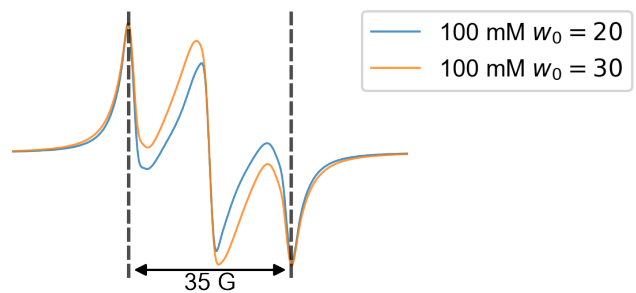


FIG. 4. Room temperature ESR (peak-normalized) of 100 mM TEMPO-SO₄ in isoctane dispersant at $w_0 = 20$ (blue) and $w_0 = 30$ (orange).

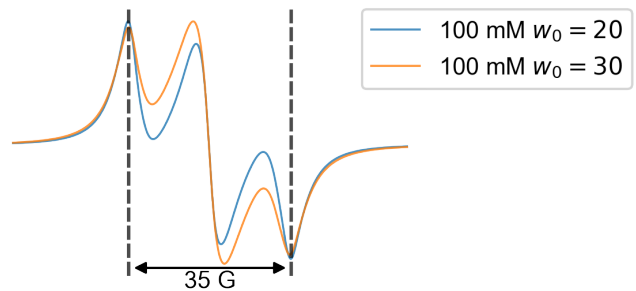


FIG. 5. Room temperature ESR (peak-normalized) of 100 mM TEMPO-SO₄ in dodecane dispersant at $w_0 = 20$ (blue) and $w_0 = 30$ (orange).

a smaller linewidth and because the amplitude of the derivative signal is inversely proportional to the square of the linewidth, the spectrum responds correspondingly dramatically to contributions from the RMs with low local concentration. The Poisson distribution predicts that lower w_0 RM mixtures will contain significantly more RM aggregates with a low local concentration (consider the number of RMs with 25 mM or 50 mM in fig. 6). In contrast, the distribution of local concentrations inside RMs with large w_0 ($w_0 = 30$ in fig. 6) peaks more sharply about a single concentration. Correspondingly, the resolved hyperfine components of the spectra contribute a smaller fraction of the overall spectrum (fig. 5 and fig. 4).

In fig. 6 a Poisson distribution predicts the distribution of local concentrations based on the average number of water molecules present in the RM. Specifically, the formula in² (which is derived from a meta-analysis of the literature) demonstrates that a RM with $w_0 = 20$ contains 4640 water molecules, so that the ratio of moles of RM aggregates per total volume of water (or aqueous solution) in the RM solution is 11.9 mM while a RM with $w_0 = 30$, due to its larger diameter of 14.75 nm, contains 17,100 water molecules and thus exhibits an aggregate to water volume ratio of only 3.25 mM. This RM aggregate:water ratio proves useful, because when the aqueous concentration of a guest molecule (such as the spin probe here) is divided by this number, it gives the aver-

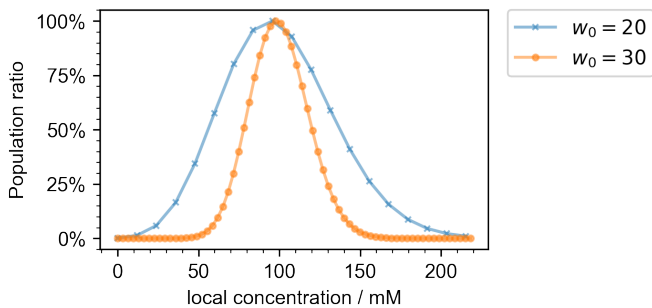


FIG. 6. Predicted percentage of RMs with each local concentration, normalized against population of most likely concentration. Note in particular how, at lower w_0 (blue line), the low-concentration portion of the distribution includes a significant number of RMs with lower concentration. At higher w_0 , the distribution is predicted to peak more tightly about the concentration of the solution before it was added to the RMs.

age number of guest molecules per RM aggregate. For example, at an aqueous concentration of 100 mM spin probe, $w_0 = 30$ RM aggregates contain an average of 30.7 spin probe molecules while $w_0 = 20$ RM aggregates contain only 8.35 spin probes.

Further investigation of Heisenberg exchange in RMs offers promise for informing on the dynamic interactions and fusion events between these nanocontainers. In particular, the differences in the fig. 5 and fig. 4 likely arise due to differing rates of fusion/fission events, which mix the local concentrations and could therefore affect the Heisenberg exchange rates. However, these considerations are reserved for future study and the following studies employ a concentration of 20 mM or less to avoid such complications.

III.2. Dramatic Variation of Spin Label Mobility with Temperature

Even a standard liquid nitrogen temperature control unit can achieve a wide enough range of temperatures to dramatically change the mobility of a spin probe inside a RM. In fact, the studies presented here explore almost the full dynamic range of standard X-band ESR experiments, as the line shapes vary from nearly isotropic three-line spectra, consistent with a spin probe freely dissolved in a viscous liquid, to spectra that are broad enough to be consistent with glassy solids. As an example, fig. 7 shows the lineshape variation exhibited by TEMPO-SO₄ inside a RM (dispersed in isooctane) that is small enough that water inside does not freeze (and thus exhibits no abrupt discontinuities of lineshape). Fig. 8 illustrates a similar variation for a CAT-16 spin label.

Existing Python libraries enable rapid development of a script that estimates the correlation time of these spectra. This script determines the field positions and amplitudes of the peaks for an entire variable-temperature experiment. It implements spline-based smoothing of the spectra in order to minimize the impact of any noise as

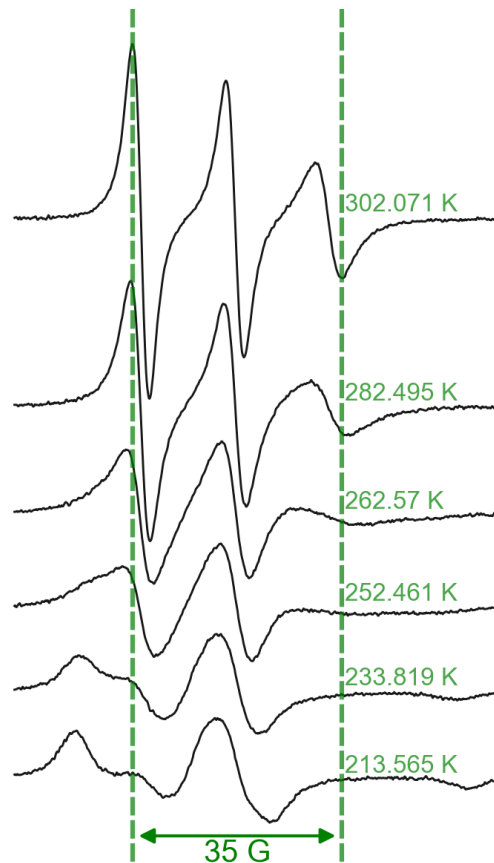


FIG. 7. ESR spectra (not normalized) of TEMPO-SO₄ in $w_0 = 3$ RMs in isooctane over a range of temperatures demonstrate an almost complete exploration of the dynamic range of X-band ESR spectroscopy.

part of this determination, making it relatively precise. Finally, it estimates the rotational correlation time (τ_c) via the classic equation^{9,20}:

$$\tau_c \approx \left(6.51 \times 10^{-10} \left(\frac{\text{s}}{\text{G}}\right)\right) \Delta B_0 \left[\sqrt{\frac{h_0}{h_{+1}}} + \sqrt{\frac{h_0}{h_{-1}}} - 2 \right] \quad (1)$$

where ΔB_0 gives the linewidth of the central line, and h_m gives the peak-to-peak height for the hyperfine transition associated with nuclear quantum number m (the three peaks $m = +1, 0, -1$ appear from low to high field, respectively). (Note that here and elsewhere, units associated with numbers are given in equations in Roman font – *e.g.* G, s, *etc.*)

This approximate measure of correlation time enables simple visualization of the change in the ESR spectra as a function of temperature. While it provides less, and more approximate, information *vs.* a simulation, it also doesn't require rigorous cross-checking of the various simulated parameters. Furthermore, it will focus on the most intense component of a multi-component spectrum. Strictly, eq. 1 strictly only accurately esti-

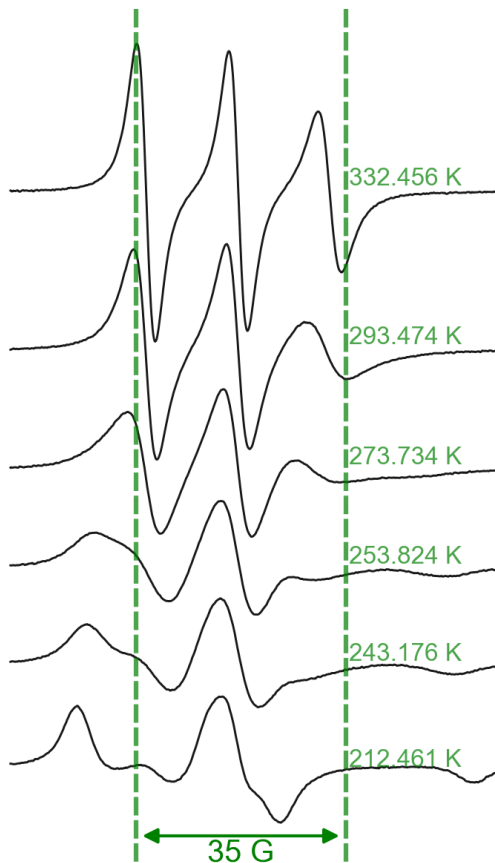


FIG. 8. ESR spectra (not normalized) of CAT-16 in $w_0 = 3$ RMs in isooctane over a range of temperatures also demonstrate an almost complete exploration of the dynamic range of X-band ESR spectroscopy.

mates the correlation time in the fast-motion regime,⁹ *i.e.* $10^{-11} < \tau_c < 3 \times 10^{-9}$ s. Nonetheless, it will also be shown that, even outside this range of applicability, eq. 1 provides a simple single number sensitive to dramatic changes in the lineshape (or lack thereof).

By exploring molecular motion over a wide temperature range, ESR can offer insight into the unusual properties of water under confinement and, in particular, how it varies with temperature. In a system such as RMs, the diffusivity of molecules varies from site to site. As a result, thermal energy excites the spin probe to different rates of rotation when it resides in a fluid aqueous medium at the core of the RM, *vs.* in the interfacial layer next to the surfactant, *vs.* in very small RMs where relatively immobile water and surfactants might rotate as a single unit inside the dispersant medium. Furthermore, in all these cases, the thermal energy needed to activate diffusion of the molecules surrounding the spin probe (water, interfacial water, or dispersant, depending on context), and thus to reduce resistance to such rotation, varies. As a result, the spectrum of the spin label rotating inside these media will respond to temperature

differently. Thus, observation of the temperature dependence of the rotational correlation time offers important insight into the energy barriers associated with transport inside nanoscopically heterogeneous materials and, in particular, offers a unique opportunity to characterize the energies required to move solvent molecules from site to site within the RM solution.

Thus, this contribution expands on the well-documented capability of ESR to measure microviscosity^{16,29,30}, and focuses on how the mobility (specifically the diffusivity) of the confined water, the dispersant, or both, responds to changes in temperature. In particular, the combination of several standard relations enables the quick characterization of the variable temperature spectra in terms of activation energies for diffusion. To begin, Stokes-Debye-Einstein (SDE):

$$\tau_c = \frac{4\pi\eta r^3}{3k_B T} \quad (2)$$

relates the correlation time (τ_c) of eq. 1, to the viscosity of the solvent (η , either water or dispersant, depending on context), where k_B is Boltzmann's constant, T is the temperature, and r is the radius of the species undergoing rotational diffusion (either the RM or the spin probe itself, depending on context). Next, to relate the translational diffusivity (D) of a particle to the viscosity of the surrounding solvent, the Einstein relation

$$\eta = \frac{k_B T}{6\pi D r_{solv}},$$

gives an expression for the viscosity of the solvent (η) in terms of its self-diffusivity (D), the radius of the solvent molecules (r_{solv}), and the temperature. Substitution of this expression into eq. 2 gives an expression showing that the correlation time is inversely proportional to the self-diffusivity of the solvent

$$\tau_c = \frac{2r^3}{9Dr_{solv}}.$$

Because the rotational diffusion quantified by τ_c and translational solvent self-diffusion quantified by D are both driven by thermal fluctuations, the $k_B T$ dependence has canceled out. The assumption that the solvent self-diffusivity obeys an Arrhenius dependence ($D \approx A \exp(-E_a/RT)$, over a limited range of temperatures) then yields

$$\tau_c = \frac{2r^3}{9Ar_{solv}} e^{+\frac{E_a}{RT}},$$

and the logarithm of both sides yields

$$\log(\tau_c) = const + \frac{E_a}{2.3026RT}, \quad (3)$$

where τ_c is the correlation time, T is the temperature, E_a is the activation energy associated with the diffusivity of

the solvent, R is the ideal gas constant, and $const$ is a constant involving a collection of terms (including the Arrhenius prefactor, A , hydrodynamic radii, *etc.*) Thus, the left-hand side of eq. 3 plotted against $1000/T$ yields a classic Arrhenius plot for the diffusivity of the solvent.

Such an Arrhenius plot of the estimated correlation time (eq. 1) experienced by a TEMPO-SO₄ inside the aqueous core of an RM dispersed in isooctane, in fig. 9, yields several unexpected results. To interpret these results, first note that one can assume that τ_c in eq. 3 decomposes into

$$\tau_c^{-1} = \tau_{RM}^{-1} + \tau_{SP}^{-1} \quad (4)$$

where τ_c gives the correlation time observed by ESR, τ_{RM} represents the correlation time associated with the rotational diffusion of the entire RM aggregate (*i.e.* assembly, *i.e.* nanocontainer) and τ_{SP} represents the correlation time for the rotational diffusion of the spin probe inside the water nanopool contained within the RM – more concretely, the rotational diffusion relative to the diffusion (or moment of inertia) frame of the RM aggregate. Importantly, when considering eq. 2 and eq. 3, the hydrodynamic radius of the spin probe and the diffusivity (viscosity) of water control τ_{SP} ; in contrast, the hydrodynamic radius of the RM aggregate and the diffusivity (viscosity) of the dispersant control τ_{RM} .

Note that w_0 controls the size of the RM aggregates: specifically, $r \approx (0.175 \text{ nm})w_0 + c$, where the constant c depends on the thickness of the surfactant^{31,32}. Therefore, RMs at the limit of low *vs.* high w_0 will approach different limiting cases of eq. 4. The limit $\tau_c \approx \tau_{RM}$, is most likely to occur for small RM sizes (small w_0) and would specifically correspond to spin labels that were fixed inside RM aggregates undergoing rotational diffusion, with the r in eq. 2 corresponding to the radius of the RM aggregate and E_a the activation energy for the diffusivity of the dispersant. In contrast, the limit $\tau_c \approx \tau_{SP}$ would correspond to large w_0 , as the larger RMs likely contain less viscous water and also exhibit slower tumbling of the RM aggregate due to their larger radius, with the r in eq. 3 corresponding to the hydrodynamic radius of the spin probe and E_a corresponding to the activation energy for the diffusion of water inside the RM.

If the $\tau_c \approx \tau_{RM}$ limit held strictly true here for the smaller RM aggregates ($w_0 = 3$), the spin probe would experience a $\tau_c \approx \tau_{RM}$ of 4.00 ns (*i.e.* $\log(\tau_c/s) = -8.398$), from eq. 2, given that the viscosity of isooctane is³³ 0.473 mPa·s at room temperature and the RM radius at $w_0 = 3$ is approximately 2.02 nm. The faster rotational correlation time reported in fig. 9 (blue) thus reflects a spin probe not totally immobilized inside the RM, likely due in part to lubrication by the water molecules. In fact, assuming the calculated $\tau_{RM} = 4.00$ ns here, and substituting the measured $\tau_c = 1.02$ ns (*i.e.* $\log(\tau_c/s) = -8.990$, blue diamonds in fig. 9) into eq. 4 yields a value of $\tau_{SP} \approx 1.37$ ns, indicating that the motion of the spin label inside the RM likely provides the primary mechanism for rotational diffusion. The slopes of the line for

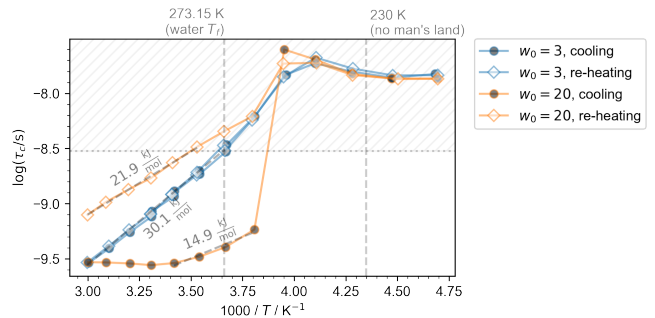


FIG. 9. Arrhenius temperature dependence for the rotational correlation time of 20 mM TEMPO-SO₄ in isooctane. Note that datapoints representing slower motion appear further up along the y -axis and that datapoints representing colder temperatures appear further to the right. The crosshatched region indicates the regime over which eq. 1 is not expected to hold quantitatively. While the correlation time of the smaller $w_0 = 3$ RM upon cooling (dark blue circles) indicates Arrhenius diffusivity of the solvent and is reproduced upon subsequent reheating of the same sample (blue diamonds), cooling of larger ($w_0 = 20$) RMs (dark gold circles) results in an abrupt transition slightly below the freezing point of water. Furthermore, the cold-shedding of the water alters the RMs so that the lineshapes upon re-heating (gold diamonds) differ significantly, as discussed in the text.

both the cooling of the $w_0 = 3$ RM (dark blue circles), and the re-heating of same sample (blue diamonds), indicate an activation energy of $E_a = 29.4$ kJ/mol. This value significantly exceeds the E_a of diffusivity of isooctane (calculated by fitting an Arrhenius plot for the literature values³⁴ of T/η to a straight line), which is 11.2 kJ/mol. Thus, this likely reflects the added energy involved in moving the lubricating water molecules that surround the spin probe in order to achieve the faster than expected correlation time.

A RM with $w_0 = 20$, in contrast, has a radius of 5.35 nm, corresponding to $\tau_{RM} \approx 73.7$ ns (*via* eq. 2) in isooctane dispersant at room temperature. Comparison of this value to fig. 9 (and keeping in mind the reciprocal addition of eq. 4) indicates that the tumbling of the RM is not a significant contributor to the τ_c experienced by the spin probe. Therefore, it is sensible to consider the limit $\tau_c \approx \tau_{SP}$, estimated with a hydrodynamic radius of 0.34 nm (*i.e.*, close to that of TEMPOL¹⁷) for TEMPO-SO₄ and the standard viscosity of water at room temperature in order to predict a τ_{SP} . These assumptions yield $\tau_c = 35.6$ ps (a similar order of magnitude as $\tau_c = 15$ ps for TEMPOL in water as noted in other literature¹⁸), which is almost an order of magnitude faster than the $\tau_c = 280$ ps (*i.e.* $\log(\tau_c/s) = -9.55$, orange diamonds in fig. 9) correlation time observed for the spin probe tumbling inside the confined water. Thus, the TEMPO-SO₄ spin probe experiences significantly greater microviscosity than one would expect for water in bulk solution. Of course, observation of such slow water under confinement or at interfaces proves largely consistent with the litera-

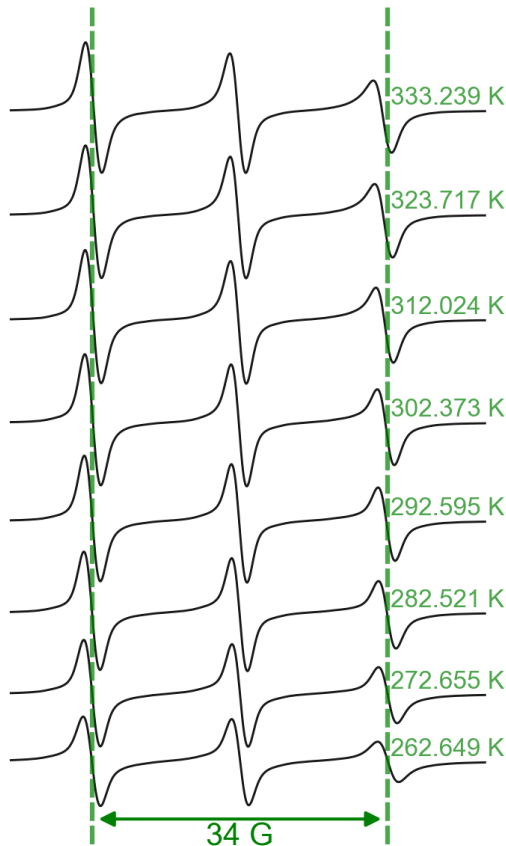


FIG. 10. ESR spectra of TEMPO-SO₄ in $w_0 = 20$ RMs in isooctane over a wide range of temperatures.

ture.

The rotational correlation time of the spin probe in the $w_0 = 20$ sample changes very little upon cooling to slightly below the freezing point of water. This lack of change over such a wide temperature range is striking. It seems to imply a very small activation energy for the diffusivity of water. However, water inside confined systems where diffusion remains relatively unrestricted in one dimension (*i.e.* inside tubes or between bundles) generally exhibits a lower limit activation energy of diffusion of 18.5 kJ/mol for bulk liquid water. Under confinement, if anything, the activation energy for the diffusion, and therefore viscosity of water, is expected to increase³⁵.

Such an unusual result invites significant speculation. One might speculate that the linewidth analysis method for assessing the correlation time fails wildly here. However, the lineshapes (fig. 10) indeed change very little with temperature. In fact, the linewidths and relative

amplitudes of the derivative peaks that reflect the molecular dynamics (see eq. 1) change very little. Only the relative field position of the three peaks change (notably the position of the rightmost peaks in fig. 10), in a fashion that suggests a change to the isotropic hyperfine constant. A changing isotropic hyperfine constant, in turn, indicates changing polarity in the environment around the nitroxide group⁷. Thus, the only significant changes to the lineshape over this extended temperature range point not to changes in spin label mobility, but rather to one of two scenarios. In the first scenario, the spin label moves from sampling more of the interfacial layer or even some of the surfactant to remaining more firmly centered inside the RM. In the second scenario, the distribution of the spin probe location within the RM remains fixed, but the average hydrogen bonding strength of the water molecules increases. Notably, either or both scenarios might actually cause the apparent lack of change of mobility over such a large temperature range (*i.e.* the very small apparent E_a). Consider, for the first scenario, the distribution of spin probe positions. In the interfacial layer, the water ostensibly moves more slowly than in the central core. If decreases in temperature localize the distribution of spin probe positions more tightly to the more fluid central core, the change of location could counteract the decreasing average mobility of the water populations as the RM is cooled. Consider, for the second scenario, that RMs are not only a pool of water, but one bounded and kept in isolation by strong interactions between the surfactant molecules^{36,7}. Temperature-driven changes to the structure of the surfactant molecules and their associated ions may help to stabilize the water structure as the temperature decreases, resulting in less disruption to the native hydrogen-bonding matrix of water, trading better surfactant-surfactant interactions for more fluid motion. Consistent with such a scenario, previous 2D ²H NMR spectroscopy have revealed that confined environments that tend to disrupt the natural mobility of water also seem to disrupt the natural hydrogen bond network². Thus, one might propose that rearrangements of the surfactant molecules that stabilize the hydrogen bond network improve the fluidity of the water enough to partially offset the decreasing temperature. Finally, before moving on from the region with apparently low E_a diffusivity, it is worth noting that something similar to the non-SDE curvature observed here has been observed previously¹⁸, where it was interpreted in terms of density fluctuations of water.

III.3. Observation of Water “Cold-Shedding”

In isooctane dispersant, once the temperature lowers slightly below the freezing point of water, the line shape changes abruptly, giving rise to the dramatic jump in fig. 9. This transition is caused by the “cold shedding” of water^{6,37}. The cold shedding alters the sample so that the ESR of the sample after reheating to room temperature appears consistent with a much smaller RM.

Various details offer clues as to the identity of this

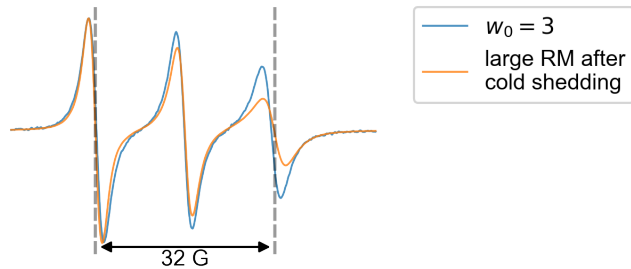


FIG. 11. ESR spectra (normalized) of 20 mM TEMPO-SO₄ in $w_0 = 3$ and a large ($w_0 = 20$) RM in isooctane. Both have been cycled below 213 K and back to 333 K temperature.

“post-shedding” RM (*i.e.* the RM that began as $w_0 = 20$, but which has changed in composition after the temperature was cycled below the freezing point and back to room temperature). As shown in fig. 11, the spectrum of the post-shedding RM exhibits a significantly greater variability in derivative peak amplitudes for the three hyperfine transitions, giving rise (via eq. 1) to the longer correlation time in fig. 9. Interestingly, the double integral of the EPR signal does not change significantly over the course of the cycle from room temperature down to cold temperatures and back to room temperature. This implies that the spin probes all integrate into the new, smaller w_0 environment rather than migrating to the end of the sample capillary with the water that is shed as ice. This combined with the long correlation time evidenced by fig. 13 indicate that the temposulfate all remains inside the RMs during the shedding process. Also interestingly, the ESR spectrum for the $w_0 = 20$ RM subject to cold shedding (fig. 11) actually exhibits a slower correlation time than the $w_0 = 3$ RM. Therefore, RM that undergoes shedding is certainly smaller than the $w_0 = 20$ RM, since it doesn’t exhibit the fast correlation time associated with fluid water. Interestingly, this smaller RM also exhibits (fig. 9) a slightly lower activation energy of diffusion than the $w_0 = 3$ RM that likely indicates the post-shedding RM is slightly larger than the $w_0 = 3$ RM and that the water lubricating the spin probe rotation experiences slightly less confinement than in the $w_0 = 3$ RM, leading to a lower activation energy.

Notably, the behavior of the (initially) $w_0 = 20$ RM contrasts with that of the $w_0 = 3$ RM, which exhibits no evidence of cold shedding, yielding the same spectra at the same temperatures during the reheating process. Note that the correlation time of the post-shedding RM may be longer than that of the $w_0 = 3$ RM for two reasons. In one possibility the post-shedding RM is smaller, and the low correlation time results from less fluid water lubricating the spin probe. In another possibility, the RM that underwent shedding is larger and any increase in water fluidity does not overcome the increase in τ_{RM} in eq. 4. A RM of $w_0 = 7$ with an RM radius of 2.72 nm results in $\tau_{RM} \approx 9.74$ ns (using eq. 2) in isooctane dispersant at room temperature. Thus, τ_{RM}^{-1}

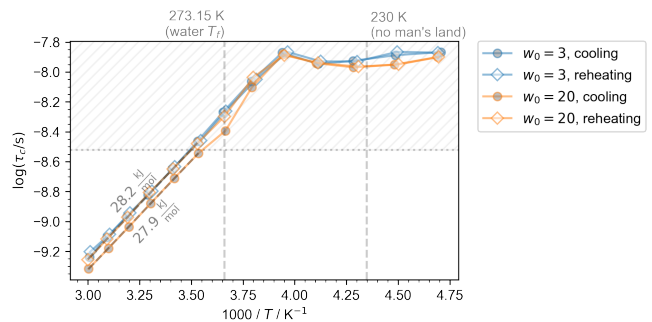


FIG. 12. Arrhenius temperature dependence of 0.5 mM CAT-16 in isooctane for ascending and descending temperature series

(*i.e.* proportional to the *rate* of rotational diffusion) decreases by only 0.148 ns^{-1} by expanding from a $w_0 = 3$ to $w_0 = 7$ RM. A change in τ_{SP}^{-1} that would compensate for this would involve increasing from the previous value of $\tau_{SP}^{-1} = 0.730 \text{ ns}^{-1}$ ($\tau_{SP} = 1.37$ ns) to $\tau_{SP}^{-1} = 0.878 \text{ ns}^{-1}$ ($\tau_{SP} = 1.14$ ns). It seems reasonable to expect such a speed-up of rotational diffusion in the less confined environment; the difference in mobility may correspond to a slight structural difference in the post-shedding micelle. While further investigations should prove straightforward, they exceed the scope of this article, which instead proceeds to analyze different label positions and dispersants.

III.4. Activation of Interfacial Water Diffusion

CAT-16 embeds in the interfacial water layer⁸ and its rotational diffusion responds to the diffusivity of water in that layer. Interestingly, at both higher and lower water loading, the correlation time observed for the interfacial water is slightly slower than that seen for a temposulfate embedded in a $w_0 = 3$ RM (tbl. II). A comparison between the data for the TEMPO-SO₄ and CAT16 spin probes can also address the question of whether the water contained in the $w_0 = 3$ RM behaves mostly as interfacial water. The CAT-16 rotation responds to an activation energy for the diffusivity of water in the interfacial layer of approximately 28 kJ/mol, similar to that observed by the $w_0 = 3$ temposulfate label (30 kJ/mol, fig. 9). Therefore, the $w_0 = 3$ RM’s water pool likely consists entirely of interfacial water molecules. Possibly, the decrease of correlation time observed with the basic method here (*i.e.*, eq. 1) upon exchanging spin probes from from temposulfate to CAT-16 in the $w_0 = 3$ RM could arise from the molecular-scale order of the CAT-16 relative to the surfactant and the likely anisotropy of its rotational diffusion tensor.

Finally, the CAT-16 data can aid in estimating the size of the post-shedding RM. Note that for the different water loadings, the correlation times do vary, consistently with what older literature has reported⁸. This variation as a function of water loading can help identify the likely water loading of the RM that has experienced shedding.

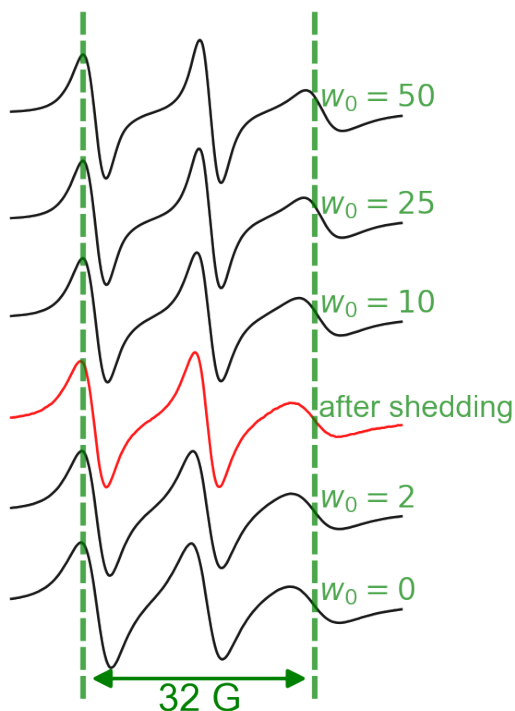


FIG. 13. ESR spectra of the spin label CAT-16 at room temperature, incorporated into AOT RMs with different water loadings (w_0). The red spectrum comes from CAT-16 that was embedded in an RM (in AOT-isooctane) that was initially $w_0 = 20$, but which was cycled below 213 K and then reheated to 293 K. As expected for cold-shedding of water, this lineshape is consistent with smaller RMs.

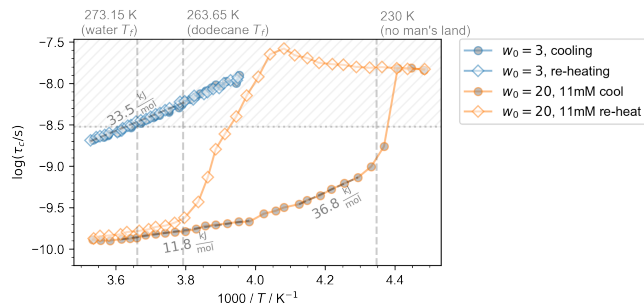


FIG. 14. Arrhenius temperature dependence of 20 mM TEMPO-SO₄ in dodecane for ascending or descending temperature series

Specifically, fig. 13 compares an (initially $w_0 = 20$) RM sample that has been subjected to water shedding to a series of RMs with different w_0 . The sample that has been subjected to shedding exhibits a lineshape most similar to an untreated sample with a low water loading of $0 < w_0 < 10$.

III.5. Freezing in Dodecane Offers Insight into Thermodynamics of Hydration Water

As previously noted, early DSC studies showed freezing of water as low as 230 K²³, while NMR studies showed freezing of water at temperatures as high as 253 K^{6,37}; with the latter result duplicated in the previous section here. The key difference between these studies appeared to be the dispersant (dodecane *vs.* isooctane, respectively). Notably, dodecane freezes at 263.65 K, so, likely, its key property is its ability to immobilize the individual RM aggregates in space and prevent fusion/fission events, without significantly altering the structure of the RM aggregates themselves. The versatility of cw ESR enables a controlled study of the dynamics inside RMs dispersed in isooctane (given in previous section) *vs.* dodecane, which follows.

These measurements of RMs in dodecane dispersant focus on a slightly lower temperature range than in isooctane, in order to enable finer temperature steps and better temperature equilibration. As for isooctane (fig. 9) RMs with $w_0 = 3$ dispersed in dodecane demonstrate a reversible series of spectra with temperature (fig. 12), with a smoothly varying correlation time. The AOT binds the water so tightly that the water cannot form ice crystals, and no freezing transition is observed. This result agrees with the DSC studies²³, which observed that water inside RMs with $w_0 < 7$ exhibits no freezing transition, even at temperatures as low as 232 K.

Swapping the isooctane dispersant for dodecane does not significantly alter the correlation time of the $w_0 = 3$ sample at 283 K ($10^{-8.70} = 2.0$ ns for both dispersants). Since the viscosities of the two dispersants differ, this result encourages the conclusion that even for these small RMs, and even though the correlation time is significantly slower than what one expects for a small spin probe dispersed in bulk water, the rotational diffusion of the spin probe inside the water encapsulated in the RM (*i.e.* $1/6\tau_{SP}$) likely exceeds (is faster) than the rotational diffusion of the RM as a whole (*i.e.* $1/6\tau_{RM}$). The activation energy of 33.5 kJ/K is similar to (only slightly exceeding) the activation energies of either the sulfate probe inside small RMs (*i.e.* $w_0 = 3$) or the activation energy of the amphiphilic Cat-16 probe that reports on the interfacial water.

Above $w_0 > 7$, DSC studies²³ have reported a freezing at approximately -41°C (approximately 232 K), with a heat of freezing roughly proportional to the number of water molecules above the $w_0 = 7$ threshold. This temperature corresponds approximately with the entry into what is commonly denoted as “no man’s land,” where ice nucleation proceeds inevitably for all non-confined environments¹. Indeed, as shown in fig. 14, the lineshape of tempo-sulfate changes dramatically as it approaches the boundary to no-man’s land. Specifically, the spin label exhibits much less mobility, consistent with sharing the nanocompartment with newly formed ice.

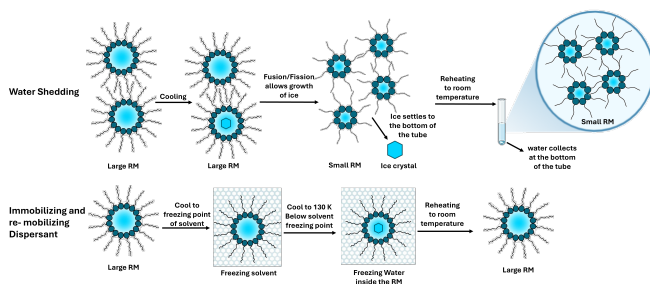


FIG. 15. Insights into ice nucleation in isooctane and dodecane. (Top) In isooctane, growth of the ice nucleus proceeds via a fusion-fission process during cooling. The ice crystals formed during cooling grow past the critical nucleus size and ultimately leave the RM (“water-shedding”). A smaller RM is left behind. Upon re-warming, the melted ice does not re-enter into the RM, but rather collects at the bottom of the ESR tube. (Bottom) In dodecane, the solvent freezing prevents the growth of embryonic ice nuclei inside the RM. This causes the water to remain supercooled until it crosses no-man’s land. During re-warming, the ice melts near 273 K, and the size of the RM remains unchanged.

III.6. Freezing in Different Dispersants Offers Insight into Nucleation

The size of the smaller RM likely corresponds to the amount of water that is not “freezable” (as opposed to non-crystallizable or unfreezable bound water). As noted previously³⁷ depends on the ionic strength of the water – which likely could be phrased as altering the composition of freezable vs. unfreezable water.

Thus, RMs are shown to be a very interesting system for studying nucleation in confined environments. The ESR data have already demonstrated support for the conclusions of older DSC²³ studies: that only the non-interfacial waters freeze. In dodecane, freezing water molecules manifest as a hysteresis in the correlation time in (gold lines in fig. 9). In isooctane, it manifests as a persistent change to the correlation times arising from the shedding of the frozen water. The $w_0 = 3$ samples do not demonstrate either of these effects, even at temperatures down to no-man’s land. In other words, several water molecules per surfactant are not “freezable” – even at temperatures below no-man’s land. Not only can the size of confinement be changed to explore the influence of the surfactant-water interface on the ability of the water molecules to freeze, but by altering the dispersant, the ability of nuclei to grow through fusion-fission of the RMs can also be controlled. Here, isooctane remains liquid over the temperature range studied, while dodecane freezes at a temperature slightly lower than bulk water. This difference significantly affects the behavior of the RMs and the freezing dynamics of the water.

In iso-octane, transient ice nuclei are allowed to grow through fusion-fission processes between different nanocontainers. Specifically, a nucleus smaller than the critical radius trapped inside a RM with no remaining “freezable” water molecules can grow to the critical size

by taking “freezable” water molecules from another RM during a fusion event. Therefore, at temperatures only tens of degrees colder than the typical freezing point of water, these growing nanocrystals of ice fall out of the RM. Without significant agitation, the water molecules cannot re-enter the RM and are thus irreversibly shed from the RM, leaving behind the surfactant and the spin probe solute.

In dodecane, the properties of the water, in terms of mobility and polarity appear quite similar. There is no evidence or reasoning that the water does not still forms the transient nuclei that, in isooctane, can grow as fusion-fission events bring new non-interfacial water molecules in contact with the embryonic ice nucleus. However, without fusion-fission events to supply the new water molecules, the small nuclei have a high free energy and quickly revert to a liquid state. This allows water to remain supercooled until it crosses the boundary into no-man’s land at which point it solidifies and requires warming to near 273 K to melt again.

This controlled comparison between the two dispersants highlights the conditions under which transient ice nuclei can grow and provides a deeper understanding of the crystallization process in confined environments. Roughly, the picture painted by these results appears consistent with critical nucleation theory^{38–40}. Interestingly, the correlation time measurements, which reflect the internal viscosity of these nanocontainers, do not appear to respond to the presence of these transient nuclei, suggesting their rarity, until possibly 244 K.

III.7. Limitations of Line Height/Width-Based Methodology

As previously noted, the rudimentary technique of eq. 1, employed in the bulk of this article, locks onto the three largest peaks in the spectrum. It, of course, ignores the possibility of multiple components.

Fig. 16 shows the spectra for RMs immobilized in dodecane, with the signal arising from temposulfate dissolved in supercooled water (the same as the dark gold circles of fig. 14). Near to 273 K, the spectrum comprises three near-Lorentzian lines, but, falling temperatures introduce an immobile component that grows progressively larger. Eventually, at temperatures approaching the crossover into no man’s land, the immobile component dominates the spectrum.

Recalling the discussion comparing between the liquid isooctane dispersant (fig. 9) and the frozen dodecane dispersant (fig. 14), this observation is tantalizing. Specifically, if transient nuclei were being formed inside the immobilized RMs, one would expect the spectra of temposulfate to reflect this to a certain degree. And this is exactly what fig. 16 provides. As the temperature grows colder and colder, the likelihood of ice nuclei formation, as well as the formation of larger-sized ice nuclei, becomes greater and greater. Consequently, the immobile component forms a greater proportion of the overall ESR spectrum.

IV. Conclusions

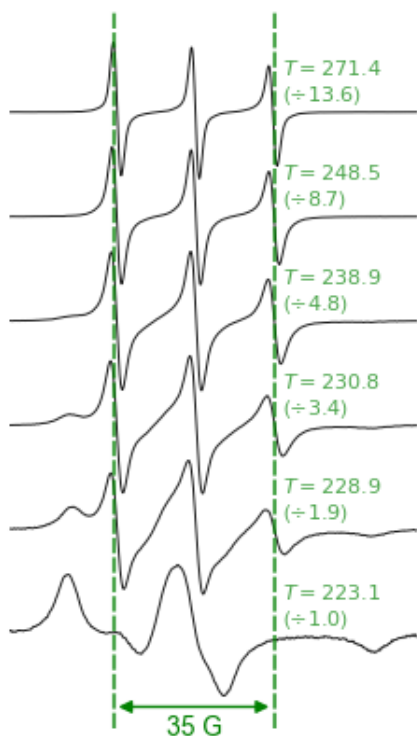


FIG. 16. Spectra of temposulfate dissolved in supercooled water confined inside RMs suspended in frozen dodecane. As the sample grows colder, an immobile component appears and grows at the expense of the mobile spectrum. Because all spectra are normalized the, normalization, the relative amplitude of each spectrum is given inside parentheses.

Another particularly interesting property of certain RM preparations (notably those in dodecane and cyclohexane) is that they can freeze, locking down the 3D translational motion of the RM aggregates. This offers the unique opportunity to create nano-compartments that remain non-interacting and spatially fixed, yet, that can be released by activating the phase transition. Here, ESR offers insight into whether or not the water and/or surfactant interface of the RM aggregates maintains some amount of rotational mobility.

While the study of supercooled water is both deep and has great breadth, it is interesting to note that this particular set of observations preliminarily could be explained with a very simplistic picture involving the transient formation of ice nuclei inside the confined environment.

The hydrogen-bonded matrix is what interacts with macromolecular systems like polymers, nanoparticles, or proteins. Macromolecules do not interact with individual water molecules but with the entire hydrogen-bonded network. The key takeaway is that the hydrogen-bonded matrix is more than the sum of its parts. While this concept isn't new, this is a specific example that highlights the crucial role of the hydrogen-bonded matrix in macromolecular chemistry.

-
- [1] “Confined water as model of supercooled water.” *Chemical Reviews*, 116:7608–7625 (2016) doi:10.1021/acs.chemrev.5b00609.
- [2] “Rapidly screening the correlation between the rotational mobility and the hydrogen bonding strength of confined water.”
- [3] “Overhauser dynamic nuclear polarization for the study of hydration dynamics, explained.” In “Biological NMR Part B,” volume 615, pages 131–175. Academic Press (2019). ISBN 978-0-12-816762-5.
- [4] “Structure and dynamics of water in polysaccharide (alginate) solutions and gels explained by the core-shell model.” *Biomacromolecules* (2024) doi:10.1021/acs.biomac.4c00447.
- [5] “Water structure and properties at hydrophilic and hydrophobic surfaces.” *Annual Review of Chemical and Biomolecular Engineering*, 11:523–557 (2020) doi:10.1146/annurev-chembioeng-120919-114657.
- [6] “Reverse micelle encapsulation as a model for intracellular crowding.” *J. Am. Chem. Soc.*, 131:8030–8039 (2009) doi:10.1021/ja901871n.
- [7] “Hydrophobic nitroxide radicals as probes to investigate the hydrophobic interaction.” *J Solution Chem*, 3:15–43 (1974) doi:10.1007/BF00649494.
- [8] “Interaction of water with sodium bis(2-ethyl-1-hexyl) sulfosuccinate in reversed micelles.” *The Journal of Physical Chemistry*, 93:7869–7876 (1989) doi:10.1021/j100360a029.
- [9] “Interfacial properties of lecithin microemulsions in the presence of lipase. a membrane spin-probe study.” *Langmuir*, 15:2375–2379 (1999) doi:10.1021/la9814236.
- [10] “Microemulsion method: A novel route to synthesize organic and inorganic nanomaterials: 1st nano update.” *Arabian Journal of Chemistry*, 5:397–417 (2012) doi:10.1016/j.arabjc.2010.09.027.
- [11] “Effect of micellar collisions and polyvinylpyrrolidone confinement on the electrical conductivity percolation parameters of water/aot/isooctane reverse micelles.” *Journal of Molecular Structure*, 1149:712–719 (2017)

- doi:10.1016/j.molstruc.2017.08.026.
- [12] “Non-equilibrium mass exchange in aot reverse micelles.” *J. Phys. Chem. B*, 124:144–148 (2020) doi:10.1021/acs.jpcc.9b08511.
- [13] “Fusion and fission inhibited by the same mechanism in electrostatically charged surfactant micelles.” *Langmuir*, 30:7947–7952 (2014) doi:10.1021/la501465v.
- [14] “How do enzymes orient when trapped on metal–organic framework (mof) surfaces?” *J. Am. Chem. Soc.*, 140:16032–16036 (2018) doi:10.1021/jacs.8b09257.
- [15] “Confinement dependence of protein-associated solvent dynamics around different classes of proteins, from the epr spin probe perspective.” *Phys. Chem. Chem. Phys.*, 24:23919–23928 (2022) doi:10.1039/D2CP03047K.
- [16] “Electron spin resonance investigation of the effects of methanol on microscopic viscosity, ordering, and polarity in different phases of ionomer membranes with sulfonated polyarylene backbones.” *Journal of Membrane Science*, 357:47–53 (2010) doi:10.1016/j.memsci.2010.03.038.
- [17] “Esr evidence for 2 coexisting liquid phases in deeply supercooled bulk water.” *Proceedings of the National Academy of Sciences*, 106:11448–11453 (2009) doi:10.1073/pnas.0900734106.
- [18] “Rotation of four small nitroxide probes in supercooled bulk water.” *J. Phys. Chem. Lett.*, 4:508–513 (2013) doi:10.1021/jz302107x.
- [19] “Characterization by electron spin resonance of reversed micelles consisting of the ternary system aot-isooctane-water.” *J. Phys. Chem.*, 92:3574–3581 (1988) doi:10.1021/j100323a050.
- [20] “Theory of esr linewidths of free radicals.” *The Journal of Chemical Physics*, 33:1094–1106 (1960) doi:10.1063/1.1731340.
- [21] “Temperature dependence of motion of a spin probe in aerosol or reversed micelles.” *Journal of Colloid and Interface Science*, 83:214–220 (1981) doi:10.1016/0021-9797(81)90026-6.
- [22] “Structural aspects in self-assembled systems of polyoxyethylene surfactants, as studied by the spin probe technique.” *Spectrochimica Acta Part A: Molecular and Biomolecular Spectroscopy*, 54:2309–2336 (1998) doi:10.1016/s1386-1425(98)00213-3.
- [23] “Characterization of water dispersion in water/sodium ethylhexylsulfosuccinate microemulsions using differential scanning calorimetry.” *J. Phys. Chem.*, 90:634–637 (1986) doi:10.1021/j100276a030.
- [24] “pyspecdata repository.”
- [25] “Nonlinear-least-squares analysis of slow-motion epr spectra in one and two dimensions using a modified levenberg-marquardt algorithm.” *Journal of Magnetic Resonance Series A*, 120:155–189 (1996).
- [26] “Aqueous 2,2,6,6-tetramethylpiperidine-n-oxyl catholytes for a high-capacity and high current density oxygen-insensitive hybrid-flow battery.” *ACS Energy Lett.*, 2:411–416 (2017) doi:10.1021/acsenergylett.6b00655.
- [27] “Epr and rheological study of hybrid interfaces in gold–clay–epoxy nanocomposites.” *Langmuir*, 30:13411–13421 (2014) doi:10.1021/la503361k.
- [28] “The interaction of small molecules with spin-labelled erythrocyte membranes.” *Biochimica et Biophysica Acta (BBA) - Biomembranes*, 219:415–427 (1970) doi:10.1016/0005-2736(70)90219-1.
- [29] “Electron spin resonance study of the ph-induced trans-formation of micelles to vesicles in an aqueous oleic acid/oleate system.” *Langmuir*, 17:4223–4231 (2001).
- [30] “Characterization of the microenvironments of alkylamidoamine-n-oxide surfactant aggregates by the epr spin labeling method.” *Journal of Solution Chemistry*, 41:1210–1223 (2012) doi:10.1007/s10953-012-9859-7.
- [31] “Determination of size parameters of water-aerosol oil reverse micelles from their nuclear magnetic resonance data.” *J. Phys. Chem.*, 88:5122–5125 (1984) doi:10.1021/j150665a064.
- [32] “Reverse micelles as hosts for proteins and small molecules.” *Biochimica et Biophysica Acta (BBA) - Reviews on Biomembranes*, 947:209–246 (1988) doi:10.1016/0304-4157(88)90025-1.
- [33] “Density and viscosity measurements of 2,2,4-trimethylpentane (isooctane) from 198 k to 348 k and up to 100 mpa.” *J. Chem. Eng. Data*, 41:1488–1494 (1996) doi:10.1021/je950191z.
- [34] “Density and viscosity measurements of 2,2,4-trimethylpentane (isooctane) from 198 k to 348 k and up to 100 mpa.” *J. Chem. Eng. Data*, 41:1488–1494 (1996) doi:10.1021/je950191z.
- [35] “Relating geometric nanoconfinement and local molecular environment to diffusion in ionic polymer membranes.” *Macromolecules*, 53:3296–3305 (2020) doi:10.1021/acs.macromol.9b02755.
- [36] “The size of aot reverse micelles.” *Journal of Physical Chemistry B*, 120:11337–11347 (2016) doi:10.1021/ACS.JPCB.6B06420.
- [37] “Dynamics of low temperature induced water shedding from aot reverse micelles.” *J. Am. Chem. Soc.*, 128:5082–5090 (2006) doi:10.1021/ja0568401.
- [38] “Heterogeneous nucleation of ice on carbon surfaces.” *J. Am. Chem. Soc.*, 136:3156–3164 (2014) doi:10.1021/ja411507a.
- [39] “Pre-ordering of interfacial water in the pathway of heterogeneous ice nucleation does not lead to a two-step crystallization mechanism.” *The Journal of Chemical Physics*, 145:211910 (2016) doi:10.1063/1.4961652.
- [40] “Is ice nucleation by organic crystals nonclassical? an assessment of the monolayer hypothesis of ice nucleation.” *J. Am. Chem. Soc.*, 143:4607–4624 (2021) doi:10.1021/jacs.0c12012.

Supplemental Materials for: Exchange and Microviscosity of Dynamic Nanocompartments

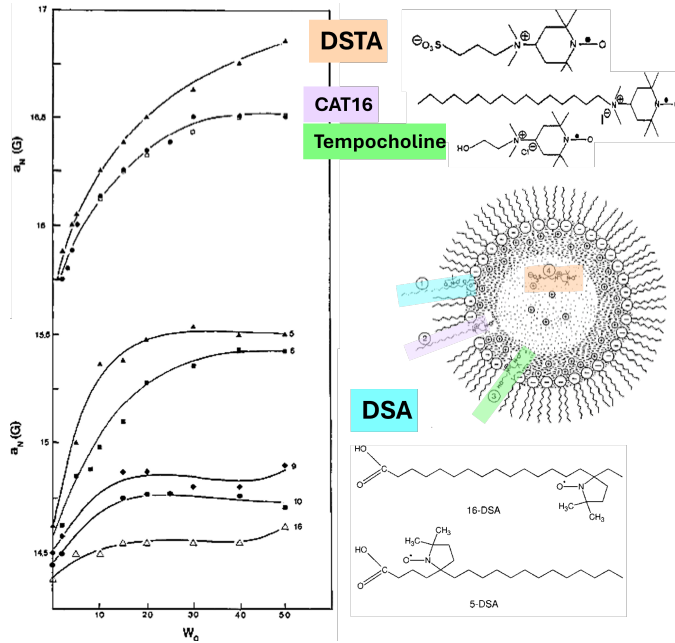


FIG. S1. Isotropic hyperfine splitting constant (a_N) in gauss as a function of water loading (W_0) for different spin labels in the AOT RM, adapted from Haering.^{S1}

S1. Supporting Information

TABLE I: correlation time (τ) of aqueous spin label DSTA and surfactant-water interface spin label CAT-16.

DSTA		CAT-16		Ratio of correlation times τ_{DSTA}/τ_{Cat16}
w_0	τ_{DSTA} / ns	w_0	τ_{Cat16} / ns	
0	5.89	0	5.29	1.11
2	2.44	2	1.55	1.57
5	1.59			
10	0.899			
50	0.308	50	1.4	0.22

S1.0.A. Characterization of Synthesized spin labels

fig. S3 and fig. S4 give the NMR spectra for both the phenylhydrazine-quenched spin labels used in this study, with a color-coding to indicate the assignment.

S1.1. Concisely Illustrating Spectral Variation over a Series

Throughout this paper, when selecting spectra out of a temperature series for presentation, a strategy for optimally choosing 6-8 temperatures was pursued. Specifically the function:

$$f(T) = \frac{\sqrt{\int \left| \frac{\partial s(B_0, T)}{\partial T} \right|^2 dB_0}}{\sqrt{\int |s(B_0, T)|^2 dB_0}}$$

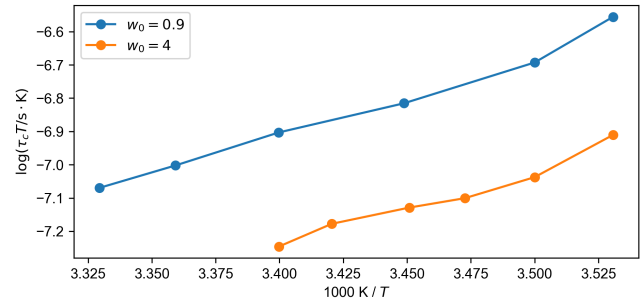


FIG. S2. Arrhenius temperature dependence for CAT 4 in $C_{12}E_4$ /cyclohexane/water system for low water loading (w_0). (Digitized and converted to arrhenius temperature dependence from the data presented in the figures by Caldaru^{S2})

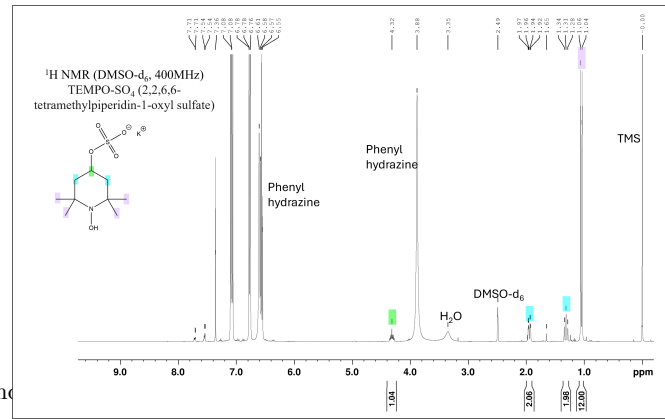


FIG. S3. NMR of TEMPO- SO_4

was developed to quantify how the shape of the spectrum ($s(B_0, T)$) varies with temperature (T). By identifying the temperatures that yield equally spaced y-values on the plot of a cumulative integral of $f(T)$, one can choose a set of representative spectra whose shape differs roughly

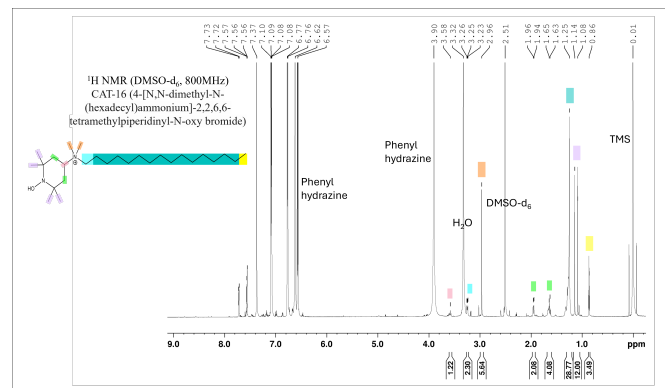


FIG. S4. NMR of CAT-16

equally from each other. For a such a strategic set of spectra at different temperatures, starting from the (previously described) lowest temperature, the best fit parameters for each fit, when employed as starting values for the fit at the next highest temperature, successfully yield high-fidelity fits for the next highest temperature in the series.

S1.2. Correlation time in post-shedding micelle.

To get a sense of the size of the post-shedding RM, we can compare the correlation time of the Cat-16 label to that in other sized RMs.

TABLE II: Correlation time (τ_c) of the spin probe CAT-16 in different water loadings, as shown in fig. 13. After the water-shedding, the red spectrum in fig. 13 shows a slower correlation time (referred to as after shedding)

w_0	CAT-16	
	τ_c / ns	
0	2.13	
2	2.05	
10	1.92	
25	1.87	
50	1.87	
after shedding	2.22	

[S1] “Characterization by electron spin resonance of reversed micelles consisting of the ternary system aot-isooctane-water.” *J. Phys. Chem.*, 92:3574–3581 (1988) doi:10.1021/j100323a050.

[S2] “Structural aspects in self-assembled systems of polyoxyethylene surfactants, as studied by the spin probe technique.” *Spectrochimica Acta Part A: Molecular and Biomolecular Spectroscopy*, 54:2309–2336 (1998) doi:10.1016/s1386-1425(98)00213-3.